



Universiteit
Leiden
The Netherlands

Warm and cold gas in low-mass protostars : Herschel Space Observatory and ground-based surveys

Yildiz, U

Citation

Yildiz, U. (2013, May 1). *Warm and cold gas in low-mass protostars : Herschel Space Observatory and ground-based surveys*. Retrieved from <https://hdl.handle.net/1887/20855>

Version: Not Applicable (or Unknown)

License: [Leiden University Non-exclusive license](#)

Downloaded from: <https://hdl.handle.net/1887/20855>

Note: To cite this publication please use the final published version (if applicable).

Cover Page



Universiteit Leiden

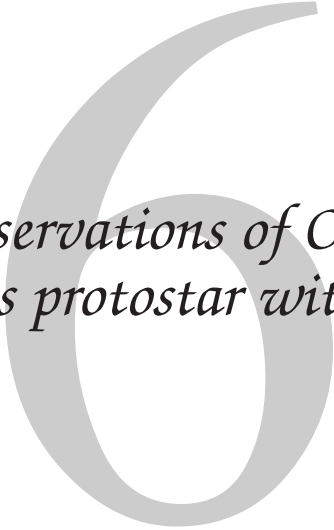


The handle <http://hdl.handle.net/1887/20855> holds various files of this Leiden University dissertation.

Author: Yildiz, Umut

Title: Warm and cold gas in low-mass protostars : Herschel Space Observatory and ground-based surveys

Issue Date: 2013-05-01



*Deep observations of O₂ toward a
low-mass protostar with Herschel*

Umut A. Yıldız, Kinsuk Acharyya, Paul F. Goldsmith, Ewine F. van Dishoeck,
Gary Melnick, René Liseau, Jo-Hsin Chen, Laurent Pagani, Edwin Bergin,
Paola Caselli, Eric Herbst, Ruud Visser, Dariusz C. Lis, Maryvonne Gerin
To be submitted to Astronomy & Astrophysics

Abstract

CONTEXT: According to traditional gas-phase chemical models, O₂ should be abundant in molecular clouds, but until recently, attempts to detect interstellar O₂ line emission with ground- and space-based observatories have failed.

AIMS: Following the multi-line detection of O₂ with low abundances in the Orion and ρ Oph A molecular clouds with *Herschel*, it is important to investigate other environments, and we here quantify the O₂ abundance near a solar-mass protostar.

METHODS: Observations of molecular oxygen, O₂, at 487 GHz toward a deeply embedded low-mass Class 0 protostar, NGC 1333 IRAS 4A, are presented, using the Heterodyne Instrument for the Far Infrared (HIFI) on the *Herschel* Space Observatory. Complementary data of the chemically related NO and CO molecules are obtained as well. The high spectral resolution data are analysed using radiative transfer models to infer column densities and abundances, and are tested directly against full gas-grain chemical models.

RESULTS: The deep HIFI spectrum fails to show O₂ at the velocity of the dense protostellar envelope, implying one of the deepest upper limits of O₂/H₂ at $\leq 6 \times 10^{-9}$ (3σ). The O₂/CO abundance ratio is less than 0.005. However, a tentative (4.5σ) detection of O₂ is seen at the velocity of the surrounding NGC 1333 molecular cloud, shifted by 1 km s⁻¹ relative to the protostar. Pure gas-phase models and gas-grain chemical models overproduce O₂ in the dense envelope, unless a long pre-collapse stage ($\sim 10^6$ years) is included, during which atomic and molecular oxygen are frozen-out onto the dust grains and fully converted into H₂O. The same model also reproduces the chemically related NO molecule if hydrogenation of NO on the grains to more complex molecules such as NH₂OH, found in recent laboratory experiments, is included. The tentative detection of O₂ in the surrounding cloud is consistent with a low density PDR model with an enhancement of the incident radiation field by a factor of ~ 500 .

CONCLUSIONS: The low O₂ abundance in the collapsing envelope around a low-mass protostar suggests that the gas and ice entering protoplanetary disks is very poor in O₂.

6.1 Introduction

Even though molecular oxygen (O_2) has a simple chemical structure, it remains difficult to detect in the interstellar medium after many years of searches (Goldsmith et al. 2011, and references therein). Oxygen is the third most abundant element in the Universe, after hydrogen and helium, which makes it very important in terms of understanding the formation and evolution of the chemistry in astronomical sources.

Pure gas-phase chemistry models suggest a steady-state abundance of $X(O_2) \approx 7 \times 10^{-5}$ relative to H_2 (e.g., Table 9 of Woodall et al. 2007), however observations show that the abundance is several orders of magnitude lower than these model predictions. Early (unsuccessful) ground-based searches of O_2 were done through the $^{16}O^{18}O$ isotopologue (Goldsmith et al. 1985, Pagani et al. 1993), for which some of the lines fall in a transparent part of the atmosphere. Due to the oxygen content of the Earth's atmosphere, it is however best to observe O_2 from space. Two previous space missions, the *Submillimeter Wave Astronomy Satellite* (SWAS; Melnick et al. 2000) and the *Odin Satellite* (Nordh et al. 2003) were aimed to detect and study interstellar molecular oxygen through specific transitions. SWAS failed to obtain a definitive detection of O_2 at 487 GHz toward nearby clouds (Goldsmith et al. 2000), whereas *Odin* observations of O_2 at 119 GHz gave upper limits of $\leq 10^{-7}$ (Pagani et al. 2003), except for the ρ Ophiuchi A cloud ($X(O_2) \sim 5 \times 10^{-8}$; Larsson et al. 2007).

The *Herschel* Space Observatory provides much higher spatial resolution and sensitivity than previous missions and therefore allows very deep searches for O_2 . Recently, *Herschel*-HIFI provided firm multi-line detections of O_2 in the Orion and ρ Oph A molecular clouds (Goldsmith et al. 2011, Liseau et al. 2012). The abundance was found to range from $X(O_2) \approx 10^{-6}$ (in Orion) to $X(O_2) \approx 5 \times 10^{-8}$ (in ρ Oph A). The interpretation of the low abundance is that oxygen atoms are frozen out onto grains and transformed into water ice that coats interstellar dust, leaving little atomic O in the gas to produce O_2 (Bergin et al. 2000). So far, O_2 has only been found in clouds where (external) starlight has heated the dust and prevents atomic O from sticking onto the grains and being processed into H_2O as predicted by theory (Hollenbach et al. 2009) or where O_2 is enhanced in postshock gas (Goldsmith et al. 2011). Not every warm cloud has O_2 , however. Melnick et al. (2012) report a low upper limit on gaseous O_2 toward the dense Orion Bar photon-dominated region (PDR).

Although the detection of O_2 in some molecular clouds is significant, these data tell little about the presence of O_2 in regions where solar systems may form. It is therefore important to also make deep searches for O_2 near solar-mass protostars to understand the origin of molecular oxygen in protoplanetary disks and eventually (exo-)planetary atmospheres. Even though the bulk of the O_2 in the Earth's atmosphere arises from life, the amount of O_2 that could be delivered by cometary impacts needs to be quantified. In the present paper, a nearby low-mass deeply embedded protostar is targeted, which has one of the largest lines of sight hydrogen column densities of $N(H_2) \sim 10^{24} \text{ cm}^{-2}$ as derived from dust modeling (Jørgensen et al. 2002, Kristensen et al. 2012). Since the *Herschel* beam size

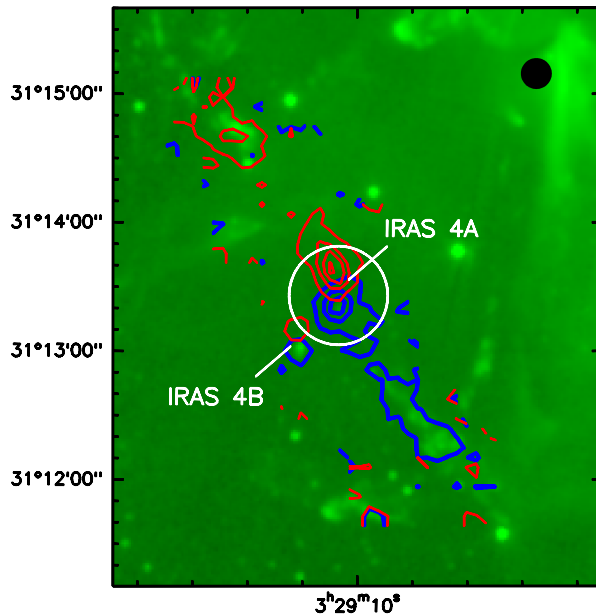


Figure 6.1 – *Spitzer*/IRAC1 (Gutermuth et al. 2008) and CO 6–5 contours (Yıldız et al. 2012) are overlaid to illustrate the NGC 1333 IRAS 4A and 4B protostars. The white circle in the center represents the observed HIFI beam of 44'' centred on IRAS 4A, illustrating that it partially overlaps with the outer part of the IRAS 4B envelope. The contours indicate the outflows, with levels starting from 3σ (15 K km s^{-1}) with an increasing step size of 6σ (30 K km s^{-1}). Blue and red velocity ranges are selected from -20 to 2.7 and from 10.5 to 30 km s^{-1} , respectively. The black dot on upper right corner shows the beam size of the CO 6–5 data.

at 487 GHz is a factor of ~ 6 smaller than that of *SWAS*, much deeper information can be obtained for these compact sources. Protostars also differ from dense clouds or PDRs by the fact that a significant fraction of the dust is heated internally by the protostellar luminosity to temperatures above those needed to sublimate O and O₂.

NGC 1333 IRAS 4A is located in the southeast part of the NGC 1333 region, together with IRAS 4B (henceforth IRAS 4A and IRAS 4B). A distance of 235 ± 18 pc is adopted based on VLBI parallax measurements of water masers in the nearby source SVS 13 (Hirota et al. 2008). Both objects are classified as deeply-embedded Class 0 low-mass protostars (André & Montmerle 1994) and are well-studied in different molecular lines such as CO, SiO, H₂O and CH₃OH (e.g., Blake et al. 1995, Lefloch et al. 1998, Bottinelli et al. 2007, Kristensen et al. 2010, Yıldız et al. 2012). Figure 6.1 shows a CO $J=6-5$ contour map obtained with APEX (Yıldız et al. 2012) overlaid on a *Spitzer*/IRAC1 ($3.6 \mu\text{m}$) image (Gutermuth et al. 2008). Both IRAS 4A and IRAS 4B have high-velocity outflows seen at different inclinations. The projected separation between the source centers of IRAS 4A and IRAS 4B is $31''$ (~ 7300 AU). The source IRAS4A was chosen for the deep O₂ search because of its chemical richness and high total column density. In contrast with

many high-mass protostars, it has the advantage that even deep spectra do not show line confusion.

On a larger scale, early millimeter observations of CO and $^{13}\text{CO } J=1-0$ by Loren (1976) and Liseau et al. (1988) found two (possibly colliding) clouds in the NGC 1333 region, with velocities separated by up to 2 km s^{-1} . Černis (1990) used extinction mapping in the NGC 1333 region to confirm the existence of two different clouds. The IRAS 4A protostellar envelope is centred at the lower velocity around $V_{\text{LSR}}=7.0 \text{ km s}^{-1}$, whereas the lower (column) density cloud appears around $V_{\text{LSR}}=8.0 \text{ km s}^{-1}$. The high spectral resolution of our data allows O_2 to be probed in both clouds. Optically thin isotopologue data of $\text{C}^{18}\text{O } 1-0$ up to $5-4$ are used to characterize the conditions in the two components. Note that these velocities do not overlap with those of the red outflow lobe, which start at $V_{\text{LSR}}=+10.5 \text{ km s}^{-1}$.

We present here the first deep observations of the $\text{O}_2 \ 3_3-1_2$ 487 GHz line towards a deeply embedded low mass Class 0 protostar observed with *Herschel*-HIFI. Under a wide range of conditions, the O_2 line at 487 GHz is the strongest line, therefore this line is selected for long integration times. The data are complemented by ground-based observations of CO isotopologues and NO using the IRAM 30m and JCMT telescopes. The CO data are used to characterize the kinematics and conditions in the clouds as well as the column of gas where CO is not frozen out. Since the O_2 ice has a very similar binding energy as the CO ice, either in pure or mixed form (Collings et al. 2004, Acharyya et al. 2007), CO provides a good reference for O_2 . NO is chosen because it is a related species that could help to constrain the chemistry of O_2 . In the gas, O_2 can be produced from atomic O through the reaction (Herbst & Klemperer 1973, Black & Smith 1984)



with rate constants measured by (Carty et al. 2006). The nitrogen equivalent of Eq. (6.1) produces NO through



The outline of the paper is as follows. Section 6.2 describes the observations and the telescopes where the data were obtained. Results from the observations are presented in Section 6.3. The deep HIFI spectrum reveals a non-detection of O_2 at the velocity of the central protostellar source. However, a tentative (4.5σ) detection is found originating from the surrounding NGC 1333 cloud at $V_{\text{LSR}}=8 \text{ km s}^{-1}$. In Section 6.3.4, radiative transfer models are used to determine the gas-phase abundance profiles of CO, O_2 and NO in the protostellar envelope, whereas full gas-grain modeling is conducted to interpret the non-detection in Section 6.4. In Section 6.5, the implications for the possible detection in the 8 km s^{-1} component are discussed and in Section 6.6, the conclusions from this work are summarized.

Table 6.1 – Overview of the observed lines.

| Molecule | Transition J_u-J_l | E_u/k_B [K] | A_{ul} [s ⁻¹] | Frequency [GHz] | Telescope/ Instrument |
|-------------------|--------------------------------|------------------|--------------------------------|--------------------|--------------------------|
| O ₂ | 3 ₃ -1 ₂ | 26.4 | 8.657×10^{-9} | 487.2492640 | <i>Herschel</i> -HIFI |
| C ¹⁸ O | 1-0 | 5.3 | 6.266×10^{-8} | 109.7821734 | IRAM 30m-EMIR |
| C ¹⁸ O | 3-2 | 31.6 | 2.172×10^{-6} | 329.3305525 | JCMT-HARP-B |
| C ¹⁸ O | 5-4 | 79.0 | 1.062×10^{-5} | 548.8310055 | <i>Herschel</i> -HIFI |
| NO (1) | 3 ₁ -2 ₁ | 19.3 | 1.387×10^{-6} | 250.8169540 | JCMT-RxA |
| NO (2) | 3 ₁ -2 ₁ | 19.3 | 1.553×10^{-6} | 250.8155940 | JCMT-RxA |
| NO (3) | 3 ₁ -2 ₁ | 19.3 | 1.849×10^{-6} | 250.7964360 | JCMT-RxA |
| NO (4) | 3 ₁ -2 ₁ | 19.3 | 4.437×10^{-7} | 250.7531400 | JCMT-RxA |

6.2 Observations

The molecular lines observed towards the IRAS 4A protostar (3^h29^m10^s.5, +31°13′30″.9 (J2000); Jørgensen et al. 2009) are presented in Table 6.1 with the corresponding frequencies, upper level energies (E_u/k_B), and Einstein A coefficients. The O₂ data were obtained with the Heterodyne Instrument for the Far-Infrared (HIFI; de Graauw et al. 2010) onboard the *Herschel* Space Observatory (Pilbratt et al. 2010), in the context of the ‘*Herschel* Oxygen Project’ (HOP) open-time key program, which aims to search for O₂ in a range of star-forming regions and dense clouds (Goldsmith et al. 2011). Single pointing observations at the source position were carried out on operation day OD 445 on August 1 and 2, 2010 with *Herschel* obsids of 1342202025-...-1342202032. The data were taken in dual-beam switch (DBS) mode in HIFI band 1a with a chop reference position located 3′ from the source position. Eight observations were conducted with an integration time of 3477 seconds each, and eight different local-oscillator (LO) tunings were used in order to allow deconvolution of the signal from the other side band. The LO tunings are shifted by 118 MHz up to 249 MHz. Inspection of the data shows no contamination from the reference position in any of the observations nor from the other side-band. The total integration time is thus 7.7 hours (27816 seconds) for the on+off source integration.

The central frequency of the O₂ 3₃-1₂ line is 487.249264 GHz with an upper level energy of $E_u=26.4$ K and an Einstein A coefficient of 8.657×10^{-9} s⁻¹ (Drouin et al. 2010). In HIFI, two spectrometers are in operation, the “Wide Band Spectrometer” (WBS) and the “High Resolution Spectrometer” (HRS) with resolutions of 0.31 km s⁻¹ and 0.073 km s⁻¹ at 487 GHz, respectively. Owing to the higher noise ranging from a factor of 1.7 up to 4.7 of the HRS compared with the WBS, only WBS observations were used for the analysis. There is a slight difference between the pointings of the H and V polarizations in HIFI, but this difference of ΔH_V (-6″.2, +2″.2; Roelfsema et al. 2012) for Band 1 is small enough to be neglected relative to the beam size of 44″ (FWHM). Spectra from both polarizations were carefully checked for differences in intensities of other detected lines but none were found. Therefore the two polarizations are averaged to improve the S/N .

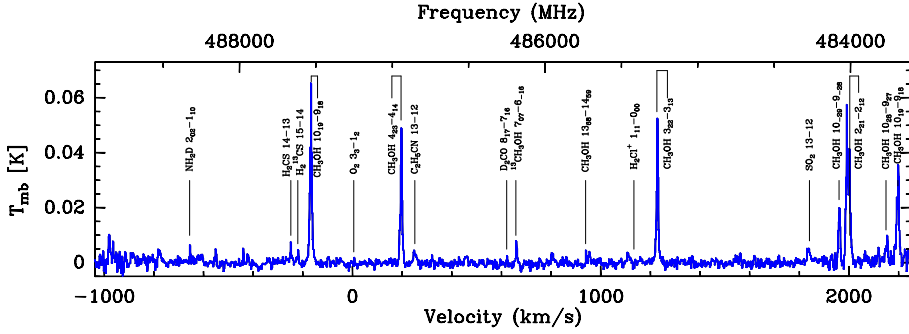


Figure 6.2 – Full spectrum taken with HIFI, with the H- and V-polarization spectra averaged. The frequency range is 488.94 GHz to 483.59 GHz from left to right. The entire bandwidth is 5.35 GHz. The O_2 line is centred near $V_{\text{LSR}}=7.0 \text{ km s}^{-1}$. A blow-up of the spectrum is presented in Fig. A.1.

Data processing started from the standard HIFI pipeline in the *Herschel* Interactive Processing Environment (HIPE¹) ver. 8.2.1 (Ott 2010), where the V_{LSR} precision is of the order of a few m s^{-1} . The lines suffer from significant standing waves in each of the observations. Therefore a special task `FitHifiFringe` in HIPE was used to remove standing waves. The fitting routine was applied to each observation one by one and it successfully removed a large part of the standing waves. Further processing and analysis was done using the GILDAS-CLASS² software. A first order polynomial was applied to all observations, which were subsequently averaged together. The standard antenna temperature scale T_A^* is corrected to main beam temperature T_{MB} by applying the efficiency of 0.76 for HIFI band 1a (Roelfsema et al. 2012, Fig. 6.2).

To understand and constrain the excitation and chemistry of O_2 , complementary transitions in NO and $C^{18}O$ are observed. Nitrogen monoxide (NO) was observed with the James Clerk Maxwell Telescope (JCMT³) by using Receiver A with a beam size of $20''$ as part of the M10BN05 observing program. The total integration time for this observation is 91 minutes. $C^{18}O$ 1–0 is observed with the IRAM 30m telescope⁴ over an area of $1' \times 1'$ with a $22''$ beam. A $C^{18}O$ 3–2 HARP-B map over $2' \times 2'$ is obtained with the JCMT with a $15''$ beam (also in Yıldız et al. 2012). Both maps are convolved to a beam of $44''$ in order to directly compare with the O_2 spectra in the same beam. Note that this convolution to a $44''$ beam is critical to reveal both the 7.0 and 8.0 km s^{-1} velocity components. The $15''$ beam spectra presented in Yıldız et al. (2012) show primarily the 7.0 km s^{-1} component.

¹ HIPE is a joint development by the Herschel Science Ground Segment Consortium, consisting of ESA, the NASA Herschel Science Center, and the HIFI, PACS and SPIRE consortia.

² <http://www.iram.fr/IRAMFR/GILDAS/>

³ The JCMT is operated by the Joint Astronomy Centre on behalf of the Science and Technology Facilities Council of the United Kingdom, the Netherlands Organisation for Scientific Research, and the National Research Council of Canada.

⁴ Based on observations carried out with the IRAM 30m Telescope. IRAM is supported by INSU/CNRS (France), MPG (Germany) and IGN (Spain).

Table 6.2 – Summary of the observed line intensities in a 44'' beam.

| Molecule | Transition | $\int T_{\text{MB}} dV$ | T_{peak} | FWHM | $\int T_{\text{MB}} dV$ | T_{peak} | FWHM | rms [mK] |
|-------------------|--------------------------------|--|-------------------|-----------------------|--|-------------------|-----------------------|------------------|
| | | [K km s ⁻¹] 7.0 km s ⁻¹ component ^a | [K] | [km s ⁻¹] | [K km s ⁻¹] 8.0 km s ⁻¹ component ^b | [K] | [km s ⁻¹] | |
| O ₂ | 3 ₃ -1 ₂ | < 0.0027 ^c | ... | ... | 0.0069 | 0.0046 | 1.3 | 1.3 ^d |
| C ¹⁸ O | 1-0 | 1.30 | 1.38 | 0.9 | 2.25 | 2.35 | 0.9 | 26 ^e |
| C ¹⁸ O | 3-2 | 1.32 | 1.36 | 0.9 | 1.67 | 1.74 | 0.9 | 99 ^e |
| C ¹⁸ O | 5-4 | 0.39 | 0.36 | 1.0 | 0.13 | 0.13 | 1.0 | 10 ^e |
| NO (3) | 3 ₁ -2 ₁ | 0.12 ^f | 0.10 ^f | 2.9 | ... | ... | ... | 46 ^e |

Notes: ^a $v_{\text{LSR}}=7.0$ km s⁻¹ component. ^b $v_{\text{LSR}}=8.0$ km s⁻¹ component. ^c 3σ upper limit. ^dIn 0.35 km s⁻¹ bins. ^eIn 0.3 km s⁻¹ bins. ^fIntensities are scaled to 44'' beam by multiplying by a factor 0.6.

The C¹⁸O 5–4 line was obtained with *Herschel*-HIFI within the “Water in Star-forming regions with *Herschel*” (WISH) guaranteed-time key program (van Dishoeck et al. 2011) in a beam size of 40'' and reported in Yıldız et al. (2012). Beam efficiencies are 0.77, 0.63, and 0.76 for the 1–0, 3–2, and 5–4 lines, respectively. The calibration uncertainty for HIFI band 1a is 15%, whereas it is 20% for the IRAM 30m and JCMT lines.

The HIFI beam size at 487 GHz of $\sim 44''$ corresponds to a 5170 AU radius for IRAS 4A at 235 pc (Fig. 6.1, white circle). It therefore overlaps slightly with the dense envelope around IRAS4B (see also Fig. 4.13; Yıldız et al. 2012) but this is neglected in the analysis. The NO data were taken as a single pointing observation, therefore the beam size is $\sim 20''$, about half of the diameter covered with the O₂ observation. In Fig. 6.13, the C¹⁸O 3–2 map is convolved to different beam sizes and corresponding intensities are measured. It is seen that the intensity decreases by a factor of 0.6 with the increasing beam size (20'' to 40''), illustrating that the IRAS 4A envelope is not a point source. Assuming that the same distribution holds for the NO emission, this same factor of 0.6 is used to scale the NO intensity to a 44'' beam.

6.3 Results

In Fig. 6.2, the full *Herschel*-HIFI WBS spectrum is presented. Although the bandwidth of the WBS data is 4 GHz, the entire spectrum covers 5.35 GHz as a result of combining eight different observations where the LO frequencies were slightly shifted in each of the settings. The rms of this spectrum is 1.3 mK in 0.35 km s⁻¹ bin, therefore many faint lines are detected near the main targeted O₂ 3₃-1₂ line. These lines include some methanol (CH₃OH) lines, together with e.g., SO₂, NH₂D, and D₂CO lines. These lines are shown in Fig. 6.12 (in the Additional materials) in detail, and are tabulated with the observed information in Table 6.6 (in the Additional materials).

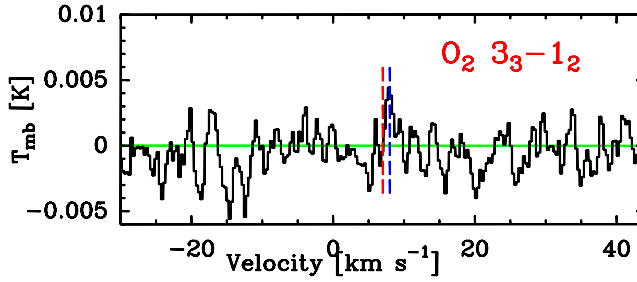


Figure 6.3 – Spectrum of Fig. 6.2 magnified around the O_2 3_3-1_2 line. The red dashed line indicates the LSR velocity of the IRAS 4A envelope at 7.0 km s^{-1} and the blue dashed line shows the velocity at 8.0 km s^{-1} .

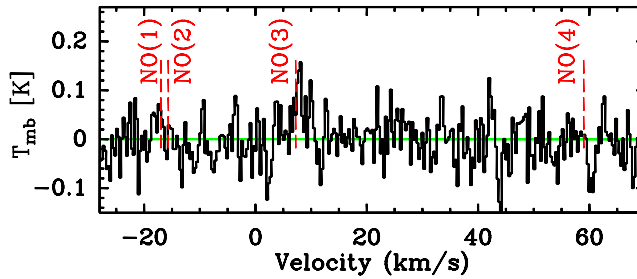


Figure 6.4 – Spectrum of the NO 3_1-2_1 transition showing the location of four hyperfine (HF) components. The spectrum is centred on the $NO(3)$ (HF) component.

6.3.1 O_2

A blow-up of the HIFI spectrum centred around the O_2 487 GHz position is presented in Fig. 6.3. The source velocity of IRAS 4A is $V_{\text{LSR}}=7.0 \text{ km s}^{-1}$ as determined from many $C^{18}O$ lines (Yıldız et al. 2012), and is indicated by the red dashed line in the figure. This spectrum of 7.7 hours integration time staring at the IRAS 4A source position is still not sufficient for a firm detection of the O_2 line at 487 GHz at the source velocity. However, a tentative detection at $V_{\text{LSR}}=8.0 \text{ km s}^{-1}$ is seen and will be discussed in more detail in Sect. 6.5.

6.3.2 NO

In Fig. 6.4, the JCMT spectrum covering the hyperfine components of the NO 3_1-2_1 transition is presented. For this specific transition, the expected ratios of the line intensities in the optically thin limit are $NO(1) : NO(2) : NO(3) : NO(4) = 75:126:200:24$. The JCMT observations have an *rms* of 40 mK in 0.3 km s^{-1} bin and 3σ emission is detected only at the intrinsically strongest hyperfine transition, $NO(3)$, with an integrated intensity

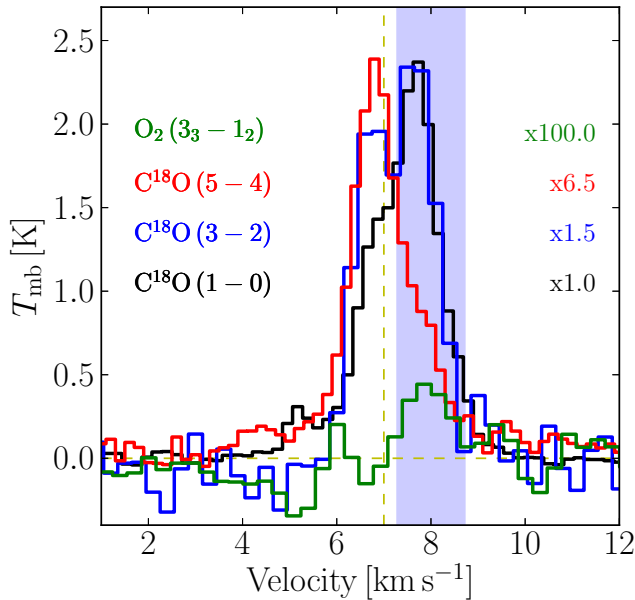


Figure 6.5 – O₂ 3₃–1₂ spectrum overplotted with the C¹⁸O 1–0, 3–2, and 5–4 lines in a 44'' beam. The C¹⁸O spectra are scaled to the same peak intensity. Note the shift in velocity from 8.0 to 7.0 km s^{−1} with increasing J .

of 0.2 K km s^{−1} centred at $V_{\text{LSR}}=7.0$ km s^{−1}. As discussed in § 6.2, this intensity is scaled by a factor of 0.6 to obtain the value in a 44'' beam. Because the data are taken in a 20'' beam, they are less sensitive to the extended 8.0 km s^{−1} component.

6.3.3 C¹⁸O

Figure 6.5 shows the C¹⁸O 1–0, 3–2, and 5–4 lines overplotted on the O₂ line. The peak of the C¹⁸O emission shifts from $V_{\text{LSR}}=8.0$ km s^{−1} to 7.0 km s^{−1} as J increases. The C¹⁸O 1–0 line is expected to come primarily from the surrounding cloud at 8.0 km s^{−1} due to the low energy of the transition ($E_{\text{up}}=5.3$ K). On the other hand, the 5–4 line has higher energy ($E_{\text{up}}=79$ K), therefore traces the warmer parts of the protostellar envelope at 7.0 km s^{−1}. As a sanity check, the ¹³CO 1–0, 3–2, and 6–5 transitions from Yıldız et al. (2012) were also inspected and their profiles are consistent with those of the C¹⁸O lines, however they are not included here due to their high opacities. The integrated intensities $\int T_{\text{mb}}dV$ for each of the 7.0 km s^{−1} and 8.0 km s^{−1} components are given in Table 6.2.

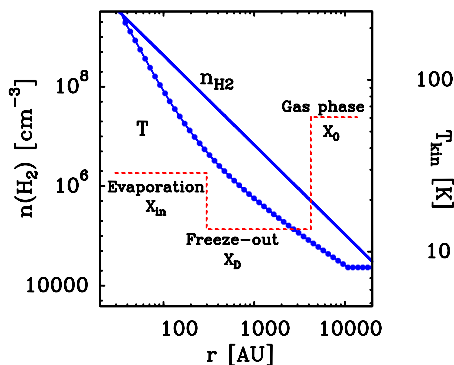


Figure 6.6 – Variation of number density and temperature of the NGC 1333 IRAS 4A envelope as function of radial distance, taken from the model of Kristensen et al. (2012). Overplotted red dashed line shows the limits of drop abundance profile obtained by the C¹⁸O modeling.

6.3.4 Column densities and abundances

6.3.4.1 Constant excitation temperature results

A first simple estimate of the O₂ abundance limit in the IRAS 4A protostellar envelope ($V_{\text{LSR}}=7.0 \text{ km s}^{-1}$ component) is obtained by computing column densities within the 44'' beam. The collisional rate coefficients for the O₂ 3₃–1₂ line give a critical density of $n_{\text{cr}}=1 \times 10^3 \text{ cm}^{-3}$ for low temperatures (Lique 2010, Goldsmith et al. 2011). The density at the 5000 AU radius corresponding to this beam is found to be $4 \times 10^5 \text{ cm}^{-3}$ based on the modeling results of Kristensen et al. (2012, see also Fig. 6.6 and below). This value is well above the critical density, implying that the O₂ excitation is thermalized. The width of the O₂ 3₃–1₂ line is taken to be similar to that of C¹⁸O, $\Delta V \approx 1.0 \text{ km s}^{-1}$. The O₂ line is assumed to be optically thin and a temperature of 30 K is used. The 3σ O₂ column density limit at $V_{\text{LSR}}=7.0 \text{ km s}^{-1}$ is then $N(\text{O}_2)=1.2 \times 10^{15} \text{ cm}^{-2}$.

The total H₂ column density of the 7.0 km s⁻¹ component in the 44'' beam is computed from the model of Kristensen et al. (2012) through

$$N_{X,\text{beam}} = \frac{\int \int n_X(z, b) dz G(b) 2\pi b db}{\int G(b) 2\pi b db}, \quad (6.3)$$

where b is the impact parameter, and $G(b)$ is the beam response function. The resulting value is $N(\text{H}_2)=2.1 \times 10^{23} \text{ cm}^{-2}$, which is an order of magnitude lower than the pencil-beam H₂ column density of $1.9 \times 10^{24} \text{ cm}^{-2}$. Using the 44''-averaged H₂ column density implies an abundance limit $X(\text{O}_2) \leq 5.7 \times 10^{-9}$. This observation therefore provides the deepest limit on the O₂ abundance observed to date. It is ~ 4 orders of magnitude lower than the chemical model predictions of $X(\text{O}_2) \sim 7 \times 10^{-5}$.

Another option is to compare the O₂ column density directly with that of C¹⁸O. These lines trace the part of the envelope where CO and, by inference, O₂ are not frozen out because of their similar binding energies (Collings et al. 2004, Acharyya et al. 2007). Using the C¹⁸O lines therefore provides an alternative constraint on the models. The integrated

Table 6.3 – Summary of column densities in a 44'' beam. See text for the conditions used for the calculations.

| Molecule | Column Density [cm ⁻²] | | Abundance w.r.t. H ₂ | |
|-----------------------------|------------------------------------|------------------------------|---------------------------------|------------------------------|
| | $N(7 \text{ km s}^{-1})^a$ | $N(8 \text{ km s}^{-1})^b$ | $X(7 \text{ km s}^{-1})^c$ | $X(8 \text{ km s}^{-1})^d$ |
| O ₂ | $<1.2 \times 10^{15}{}^e$ | $(2.8 - 4.3) \times 10^{15}$ | $<5.7 \times 10^{-9}$ | $(1.3 - 2.1) \times 10^{-8}$ |
| C ¹⁸ O | $(3.5 - 6.3) \times 10^{14}$ | $(1.8 - 2.3) \times 10^{15}$ | $(3.5 - 6.2) \times 10^{-7}$ | ... |
| NO | 4.0×10^{14} | ... | 1.9×10^{-9} | ... |
| H ₂ ^f | 2.1×10^{23} | $1 \times 10^{22}{}^f$ | ... | ... |

Notes: ^aColumn density of the bin at 7.0 km s⁻¹, a.k.a. non-detection. ^bColumn density of the bin at 8.0 km s⁻¹, a.k.a. tentative detection. ^c $V=7.0 \text{ km s}^{-1}$ component. ^d $V=8.0 \text{ km s}^{-1}$ component. ^e 3σ column density. ^fBeam averaged H₂ column density in a 44'' beam. Computed using $\text{CO}/\text{H}_2 = 10^{-4}$ and $\text{CO}/\text{C}^{18}\text{O} = 550$ (Wilson & Rood 1994).

intensity ratio of C¹⁸O 5–4/3–2 is equal to 0.29 for the 7.0 km s⁻¹ component. This ratio can then be analysed using the RADEX non-LTE excitation and radiative transfer program (van der Tak et al. 2007) to constrain the physical parameters. Figure 6.14 (in the Additional Materials) presents the integrated intensity ratios as function of temperature and density, obtained for optically thin conditions. The observed ratios are indicated in dash-dotted lines. Using a minimum density of $\sim 4 \times 10^5 \text{ cm}^{-3}$ for the envelope within the 44'' beam (shown by the purple vertical line) implies a kinetic temperature of $\sim 20\text{--}30 \text{ K}$ from the 5–4/3–2 ratio, consistent with the CO sublimation temperature (gas and dust temperature are coupled at these high densities).

For these physical conditions, the absolute C¹⁸O 3–2 and 5–4 line intensities imply a C¹⁸O column density range of $(3.5\text{--}6.3) \times 10^{14} \text{ cm}^{-2}$. The corresponding abundance ratio is $N(\text{O}_2)/N(\text{C}^{18}\text{O})=2.6 \pm 0.7$, so $N(\text{O}_2)/N(\text{CO})=(4.9 \pm 1.5) \times 10^{-3}$ assuming $\text{CO}/\text{C}^{18}\text{O}=550$. The column densities and O₂ abundances which are associated with the protostellar source at $V_{\text{LSR}} = 7.0 \text{ km s}^{-1}$ are summarized in Table 6.3.

The critical density for the NO transition is higher than that for O₂ or CO, so analysis requires a non-LTE excitation calculation using RADEX. For the detected NO (3) line diluted by a factor of 0.6, the inferred column density within 44'' is $N(\text{NO})=4 \times 10^{14} \text{ cm}^{-2}$, assuming $T_{\text{kin}}=30 \text{ K}$ and $n(\text{H}_2)=4 \times 10^5 \text{ cm}^{-3}$. For these conditions, the NO lines are optically thin. Thus, the implied NO abundance is $N(\text{NO})/N(\text{H}_2)=X(\text{NO})=1.9 \times 10^{-9}$ and $N(\text{NO})/N(\text{O}_2) \geq 0.33$. The inferred column density is nearly identical if the analysis is carried out for a 20'' beam, since the higher density at the edge of a 20'' beam ($n=1.5 \times 10^6 \text{ cm}^{-3}$) compensates for the lack of beam dilution.

6.3.4.2 Drop abundance models

The above analysis assumes constant physical conditions along the line of sight as well as constant abundances. It is well known from multi-line observations of C¹⁸O that the

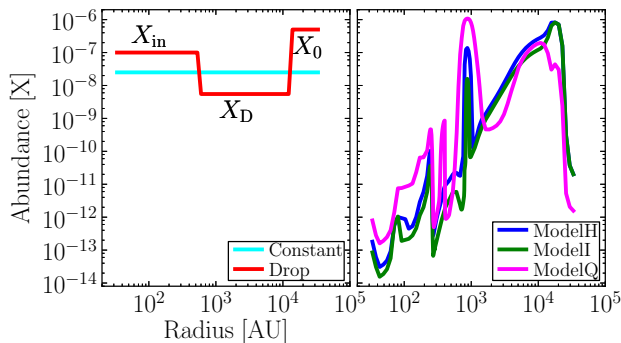


Figure 6.7 – *Left*: schematic diagram showing the best-fit drop abundance profile of O_2 following the C^{18}O profile (red line) and constant abundance profile (light blue); and *right*: best-fit profiles obtained via dust-grain modeling (other colored lines).

CO abundance varies throughout the envelope, dropping by more than an order of magnitude in the cold freeze-out zone (e.g., Jørgensen et al. 2002, Yıldız et al. 2010, 2012). A more sophisticated analysis of the O_2 abundance is therefore obtained by using a model of the IRAS 4A envelope in which the density and temperature vary with position. The envelope structure presented in Fig. 6.6 has been quantified by modeling the continuum emission (both the spectral energy distribution and the submillimeter spatial extent) using the 1D spherically symmetric dust radiative transfer code DUSTY (Ivezić & Elitzur 1997). A power-law density profile is assumed with an index p , i.e., $n \propto r^{-p}$, and the fitting method is described in Schöier et al. (2002) and Jørgensen et al. (2002, 2005b), and is further discussed in Kristensen et al. (2012). The temperature is calculated as function of position by solving for the dust radiative transfer through the assumed spherical envelopes, given the luminosity of the source. The gas temperature is assumed to be equal to the dust temperature. IRAS 4A is taken to be a standalone source; the possible overlap with IRAS 4B is ignored.

The observed line intensities are used to constrain the molecular abundances in the envelope by assuming a trial abundance structure and computing the non-LTE excitation and line intensities with radiative transfer models for the given envelope structure. For this purpose, the Monte Carlo line radiative transfer program RATRAN (Hogerheijde & van der Tak 2000) is employed. The simplest approach assumes a constant O_2 abundance through the envelope. Figure 6.7 (*left*) shows different abundance profiles whereas Fig. 6.8 (*top left*) shows the resulting line intensities overplotted on the observed O_2 line. The light blue line is the maximum constant O_2 abundance that can be hidden in the noise, which is 2.5×10^{-8} . This is within a factor of 4 of the simple column density ratio estimate.

A more realistic abundance structure includes a freeze-out zone below 25 K where both O_2 and CO are removed from the gas. Such a CO ‘drop’ abundance profile has been determined for the IRAS 4A envelope via the optically thin C^{18}O lines from 1–0 to 10–

9 in Yıldız et al. (2012). By using the best fit CO abundance structure and assuming a constant O₂/CO abundance ratio, a best fitting value of O₂/C¹⁸O ≤ 1 is obtained (red line), corresponding to O₂/CO < 2 × 10⁻³.

In summary, both the simple column density estimate and the more sophisticated envelope models imply a maximum O₂ abundance of ~ 10⁻⁸, an O₂/CO ratio of ≤ 5 × 10⁻³.

6.4 Gas-grain models for the protostellar envelope

The next step in the analysis is to compare the upper limit for the $V_{\text{LSR}}=7.0 \text{ km s}^{-1}$ component with full gas-grain chemical models. The Ohio State University gas-grain network (Garrod et al. 2008) is used as the basis for the chemical network, which contains an extensive gas-grain chemistry. There are 590 gas phase and 247 grain surface species and 7500 reactions among them. In the subsequent sub-sections, various chemical processes that were considered in the network and are relevant for O₂ and NO are discussed.

6.4.1 Gas phase O₂ and NO formation

In the gas, O₂ is predominantly formed via reaction (6.1) between O atoms and OH radicals. The rate coefficient of the above reaction has been measured in the temperature range between 39 K and 142 K with the CRESU (Cinétique de Réaction en Écoulement Supersonique Uniforme) technique by Carty et al. (2006) who found a rate coefficient of $3.5 \times 10^{-11} \text{ cm}^3 \text{ s}^{-1}$ that is constant with temperature. However, several theoretical calculations, especially below 39 K, also exist in the literature. Using quantum mechanical calculations with the so-called J -shifting approximation and neglecting non-adiabatic coupling, Xu et al. (2007) obtained a rate coefficient that decreases as the temperature drops from 100 to 10 K. At 10 K, the computed rate coefficient has fallen to a value of $5.4 \times 10^{-13} \text{ cm}^3 \text{ s}^{-1}$, significantly lower than the 39 K experimental value. However, more recent calculations by Lin et al. (2008), in which the J -shifting approximation has been removed, find a rate coefficient at 10 K of $7.8 \times 10^{-12} \text{ cm}^3 \text{ s}^{-1}$, higher than the Xu et al. (2007) value but still only about 1/4.5 of the experimental value at 39 K. Various O₂ formation rates are listed in Table 6.4. We have used all three rate coefficients in order to match the observed O₂ abundance.

Gas-phase NO is predominantly formed through reaction (6.2). Its gas-phase reaction rate coefficient is listed in Table 6.4. This reaction is taken from the OSU database and was first determined by Smith et al. (2004).

Table 6.4 – Rate coefficients for O₂ (Equation 6.1) and NO (Equation 6.2) formation.

| No. | Species | T [K] | Rate coeff. [$\text{cm}^3 \text{s}^{-1}$] | References |
|-----------------|----------------|---------|---|---------------------|
| 1. ^a | O ₂ | 39–149 | 3.5×10^{-11} | Carty et al. (2006) |
| 2. ^b | O ₂ | 10 | 7.8×10^{-12} | Lin et al. (2008) |
| 3. ^c | O ₂ | 10 | 5.4×10^{-13} | Xu et al. (2007) |
| 4. | O ₂ | ... | $7.5 \times 10^{-11} (T/300)^{-0.25}$ | OSU database |
| 5. | NO | ... | $7.5 \times 10^{-11} (T/300)^{-0.18}$ | OSU database |

Notes: ^aCRESU measurement ^bwithout J -shifting ^cwith J -shifting

6.4.2 Grain chemistry specific to O₂ and NO

The grain surface chemistry formulation in the OSU code follows the general description by Hasegawa & Herbst (1993) for adsorption, diffusion, reaction, dissociation and desorption processes, updated and extended by Garrod et al. (2008). The binding energies of various species to the surface are critical parameters in the model. In most of the models, we adopt the binding energies from Garrod & Herbst (2006) appropriate for a water-rich ice surface. However, the possibility of a CO-rich ice surface is also investigated by reducing the binding energies by factors of 0.75 and 0.5, respectively (Bergin et al. 1995, Bergin & Langer 1997).

The presence of O₂ on an interstellar grain can be attributed to two different processes. First, gas phase O₂ can be accreted on the grain surface during the (pre-)collapse phase and second, atomic oxygen can recombine to form O₂ on the dust grain via the following reaction:



Following Tielens and Hagen (1982), 800 K is used as the binding (desorption) energy for atomic oxygen on water ice. For O₂, its binding energy on water ice is taken as 1000 K following Cuppen & Herbst (2007), which is an average value obtained from the TPD data by Ayotte et al. (2001) and Collings et al. (2004). A ratio of 0.5 between the diffusion barrier and desorption energy has been assumed for the entire calculation (Cuppen & Herbst 2007), so the hopping energy for atomic oxygen is 400 K.

For this hopping energy, one oxygen atom requires 2×10^5 seconds to hop to another site at 10 K. For comparison, the time needed for a hydrogen atom to hop to another site is around 0.35 second, which is at least a factor of 10^6 faster. Therefore, instead of forming O₂, an accreted atomic oxygen species will get hydrogenated, leading to the formation of OH and H₂O. Therefore it is most unlikely that accreted atomic oxygen will produce any significant amount of O₂ on the grain surface during the pre-collapse phase. Recent studies using the continuous time random walk (CTRW) Monte Carlo method do not produce significant O₂ on the grain surface (Cuppen & Herbst 2007). However, elevated grain temperatures ($\gtrsim 30$ K), when the residence time of an H atom on the grain is very short and atomic oxygen has enhanced mobility, could be conducive to O₂ formation.

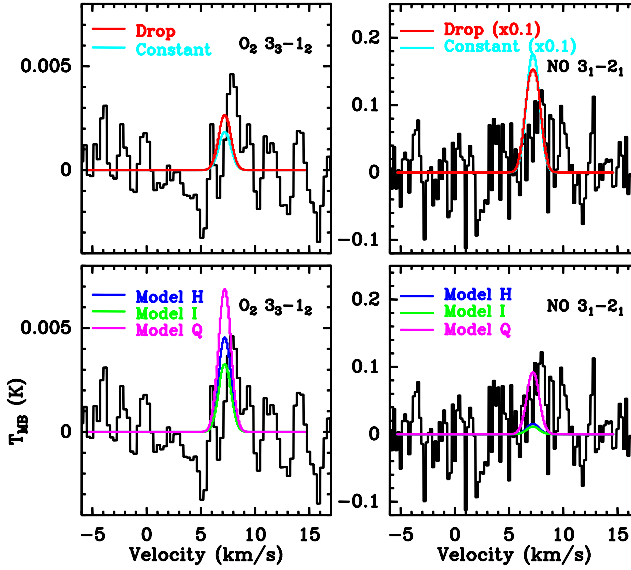
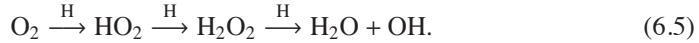


Figure 6.8 – Best-fit model spectra produced by different abundance profiles for O₂ 3₃–1₂ and NO (3) 3₁–2₁ are overlotted over the observed spectra. For NO, Case 2 is adopted.

What happens to the O₂ that is formed in the gas phase and accreted onto the dust grains? There are two major destruction pathways. First, the reaction of O₂ with atomic H leads to the formation of HO₂ and H₂O₂, which then could be converted to water following reaction pathways suggested by Ioppolo et al. (2008) and Cuppen et al. (2010):



Thus, a longer cold pre-collapse phase would significantly reduce O₂ on the dust grains and turn it into water ice, whereas a shorter pre-collapse phase would yield a higher solid O₂ abundance (Roberts & Herbst 2002).

The second destruction route leads to the formation of ozone through



This route is most effective at slightly higher grain temperatures when atomic oxygen has sufficient mobility to find an O₂ molecule before it gets hydrogenated. Ozone could also be hydrogenated as suggested by Tielens & Hagen (1982) and confirmed in the laboratory by Mokrane et al. (2009) and Romanzin et al. (2010):



Similarly, accreted NO on the grain surface can undergo various reactions. In particular, recent laboratory experiments have shown that NO is rapidly hydrogenated to NH₂OH at

low ice temperatures (Congiu et al. 2012). A critical parameter here is the competition of the different channels for reaction of $\text{HNO} + \text{H}$, which can either go back to $\text{NO} + \text{H}_2$ or form H_2NO .

The final important ingredient of the gas-grain chemistry is the rate at which molecules are returned from the ice back into the gas phase. Both thermal and non-thermal desorption processes are considered. The first non-thermal process is reactive desorption; here the exothermicity of the reaction is channeled into the desorption of the product with an efficiency determined by a parameter a_{RRK} (Garrod et al. 2007). In these model runs, a value of 0.01 is used, which roughly translates into an efficiency of 1%. Recently, Du et al. (2012) used 7% for the formation of H_2O_2 .

Second, there is desorption initiated by UV absorption. Photodissociation of an ice molecule produces two atomic or radical products, which can subsequently recombine and desorb via the reactive desorption mechanism. The photons for this process derive both from the external radiation field and from UV photons generated by ionization of H_2 due to cosmic rays, followed by the excitation of H_2 by secondary electrons. The externally generated UV photons are very effective in diffuse and translucent clouds but their role in dense clouds is limited to the edge of the core (Ruffle & Herbst 2000, Hollenbach et al. 2009). The cosmic-ray-generated internal photons can play an effective role in the dense envelope, with a photon flux of $\approx 10^4$ photons $\text{cm}^{-2} \text{s}^{-1}$ (Shen et al. 2004). We have considered both sources of radiation in our model. In either case, the rate coefficients for photodissociation on surfaces are assumed to be the same as in the gas phase.

Photodesorption can proceed both by the recombination mechanism described above as well as by kick-out of a neighboring molecule. The combined yields for a variety of species including CO and H_2O have been measured in the laboratory (Öberg et al. 2009a,b, Muñoz Caro et al. 2010) and computed through molecular dynamics simulations for the case of H_2O by Andersson & van Dishoeck (2008) and Arasa et al. (2010). Finally, there is the heating of grains via direct cosmic ray bombardment, which is effective for weakly bound species like CO and O_2 and included following the formulae and parameters of Hasegawa & Herbst (1993).

6.4.3 Model results

Our physical models have two stages, the “pre-collapse stage” and the “protostellar stage”. In the pre-collapse stage, the hydrogen density is $n_{\text{H}}=10^5 \text{ cm}^{-3}$, visual extinction $A_{\text{V}}=10$ mag, the cosmic-ray ionization parameter, $\zeta=1.3\times 10^{17} \text{ s}^{-1}$, and the (gas and grain) temperature, $T=10 \text{ K}$, which are standard parameters representative of cold cores. The initial elemental abundances of carbon, oxygen and nitrogen are 7.30×10^{-5} , 1.76×10^{-4} and 2.14×10^{-5} , respectively, in the form of atomic C^+ , O and N . All hydrogen is assumed to be in molecular form initially. In the second stage, the output abundance of the first phase is used as the initial abundance at each radial distance with the density, temperature

Table 6.5 – Chemical models considered for the IRAS 4A protostellar envelope

| Model | Pre-collapse stage [yr] | Protostellar stage [yr] | O ₂ formation rate [cm ³ s ⁻¹] | $T_{\text{peak}}(\text{O}_2)^a$ [K] | $T_{\text{peak}}(\text{NO})^a$ [K] |
|----------------------|-------------------------|-------------------------|--|-------------------------------------|------------------------------------|
| <i>A</i> | 5×10^4 | 10^5 | $7.5 \times 10^{-11} (T/300)^{-0.25}$ | 0.119 | ... |
| <i>B</i> | 1×10^5 | 10^5 | $7.5 \times 10^{-11} (T/300)^{-0.25}$ | 0.102 | ... |
| <i>C</i> | 2×10^5 | 10^5 | $7.5 \times 10^{-11} (T/300)^{-0.25}$ | 0.085 | ... |
| <i>D</i> | 3×10^5 | 10^5 | $7.5 \times 10^{-11} (T/300)^{-0.25}$ | 0.073 | ... |
| <i>E</i> | 5×10^5 | 10^5 | $7.5 \times 10^{-11} (T/300)^{-0.25}$ | 0.042 | ... |
| <i>F</i> | 6×10^5 | 10^5 | $7.5 \times 10^{-11} (T/300)^{-0.25}$ | 0.024 | ... |
| <i>G</i> | 7×10^5 | 10^5 | $7.5 \times 10^{-11} (T/300)^{-0.25}$ | 0.011 | ... |
| <i>H^b</i> | 8×10^5 | 10^5 | $7.5 \times 10^{-11} (T/300)^{-0.25}$ | 0.0045 | 0.015 |
| <i>I^b</i> | 1×10^6 | 10^5 | $7.5 \times 10^{-11} (T/300)^{-0.25}$ | 0.0032 | 0.011 |
| <i>J</i> | 8×10^4 | 2×10^4 | 3.50×10^{-11} | 0.106 | ... |
| <i>L</i> | 3×10^5 | 10^5 | 3.50×10^{-11} | 0.063 | ... |
| <i>M</i> | 3×10^5 | 10^5 | 7.84×10^{-12} | 0.047 | ... |
| <i>N</i> | 3×10^5 | 10^5 | 5.40×10^{-13} | 0.018 | ... |
| <i>O</i> | 5×10^5 | 10^5 | 3.50×10^{-11} | 0.031 | ... |
| <i>P</i> | 5×10^5 | 10^5 | 7.84×10^{-12} | 0.020 | ... |
| <i>Q^b</i> | 5×10^5 | 10^5 | 5.40×10^{-13} | 0.0068 | 0.091 |

Notes: ^aRATRAM model results using a line width of 1.0 km s⁻¹. ^bBest fit models. For NO, Case 2 is tabulated.

and visual extinction parameters at each radius taken from the IRAS 4A model shown in Fig. 6.6. We assume that the transition to the protostellar phase from the pre-collapse stage is instantaneous i.e., the power-law density and temperature structure are established quickly, consistent with evolutionary models (Lee et al. 2004, Young & Evans 2005).

To explain the observed abundance profile of O₂, both the pre-collapse time and protostellar time as well as the O₂ formation rates are varied. Analysis of CO and HCO⁺ multi-line observations in pre- and protostellar sources have shown that the high density pre-collapse stage lasts typically a few $\times 10^5$ yr (e.g., Jørgensen et al. 2005b, Ward-Thompson et al. 2007). The models *A* to *Q* have different parameters and timescales which are listed in Table 6.5. Those models result in abundance profiles in the envelope at each time step and radius. These profiles are then run in RATRAM in order to compare directly with observations.

Figure 6.7 (*right*) shows examples of model abundance profiles whereas Fig. 6.8 (*bottom left*) presents the comparison between model line emission and data. Table 6.5 summarizes the resulting O₂ peak temperatures for each of the models. All models except *H*, *I*, and *Q* overproduce the observed O₂ emission of at most a few mK, by up to two orders of magnitude in peak temperature. The models that are consistent with the data have in common longer pre-collapse stages; in particular Model *I*, which has the longest pre-collapse stage of 10^6 years, best fits the 3σ O₂ limit.

For NO, the *H*, *I*, and *Q* models were calculated twice. In Case 1, hydrogenation of HNO leads back to NO and H₂ and in Case 2 hydrogenation of HNO leads to H₂NO as sug-

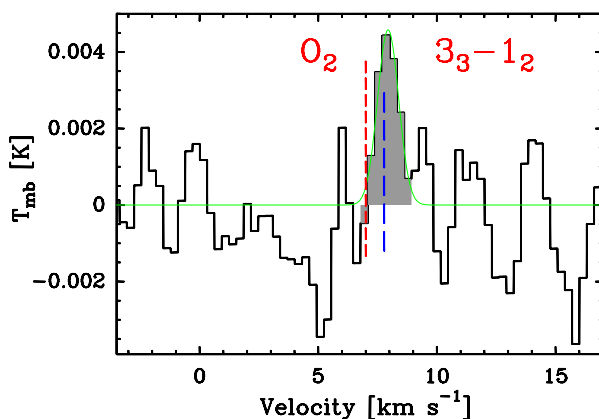


Figure 6.9 – Tentative detection of the O₂ 3₃-1₂ line from the extended NGC 1333 cloud. The red line indicates the source velocity of IRAS 4A at 7.0 km s⁻¹ and the blue line indicates the extended cloud V_{LSR} at 8.0 km s⁻¹. Green line indicates a Gaussian fit to the component at 8.0 km s⁻¹.

gested by Congiu et al. (2012). Comparison of the results from Case 1 with observations shows significant overproduction of the observed NO emission of 0.1 K, whereas Case 2 underproduces NO. Therefore, a combination of both reactions appears to be needed.

These results for IRAS 4A suggest that a long pre-collapse stage is characteristic of the earliest stages of star formation, in which atomic and molecular oxygen are frozen-out onto the dust grains and converted into water ice, as proposed by Bergin et al. (2000). Similarly, the rapid conversion of NO to other species on the grains limits its gas-phase abundance. It is clear that the grain surface processes are much more important than those of the pure gas-phase chemistry in explaining the O₂ and NO observations.

The model results show that the fraction of O₂ or NO left on the grains must indeed be very small, dropping to $\leq 10^{-9}$ close to the protostar (Fig. 6.8, right). This in turn implies that the gas and ice that enter the disk are very poor in O₂. Although IRAS 4A is the only low-mass protostar that has been observed to this depth, the conclusions drawn for IRAS 4A probably hold more generally. Thus, unless there is significant production of O₂ in the disk, the icy planetesimals will also be poor in O₂.

6.5 Tentative detection of O₂ in the 8 km s⁻¹ cloud

Although there is no sign of O₂ emission at the velocity of the dense protostellar envelope (7.0 km s⁻¹), a 4.5 σ tentative detection of O₂ 3₃-1₂ line emission is found at V_{LSR}=8.0 km s⁻¹, the velocity of the more extended NGC 1333 molecular cloud (Fig. 6.9 Loren 1976, Liseau et al. 1988). The peak intensity of the tentative detection is T_{mb}=4.6 mK, the line width $\Delta V=1.3$ km s⁻¹, and the integrated intensity is $\int T_{mb}dV=6.9$ mK km s⁻¹

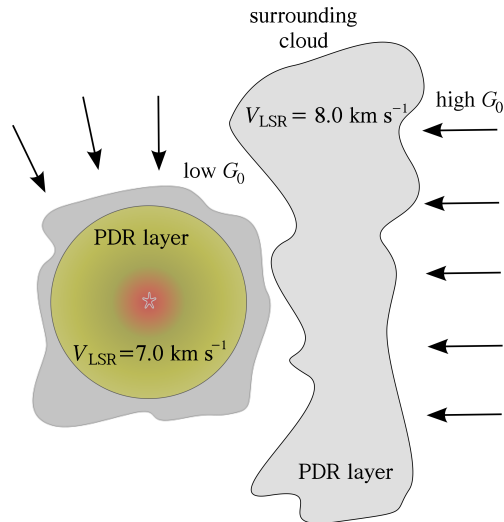


Figure 6.10 – Schematic cartoon showing the scenario of O₂ emission originating from the surrounding cloud.

between the velocities of 6.5 to 9.7 km s⁻¹. The large HIFI beam size of 44'' encompasses both the extended cloud as well as the compact envelope. Since any O₂ emission is optically thin, the two components cannot block each other, even if slightly overlapping in velocity. Figure 6.10 shows a possible schematic geometry for the protostar and the surrounding cloud.

The density in the surrounding cloud at 8.0 km s⁻¹ is expected to be significantly lower than that in the envelope. Figure 6.14 (in the Additional Materials) includes the C¹⁸O 3–2/1–0 ratio for the 8.0 km s⁻¹ component. The observed value is consistent with a wide range of kinetic temperatures from 20 K to 70 K, with corresponding densities in a narrow range from 7×10^3 to 2×10^3 cm⁻³, respectively. C¹⁸O column densities from the 3–2 and 1–0 line intensities are then $(1.8\text{--}2.3) \times 10^{15}$ cm⁻² for this range of physical parameters.

For the same range of conditions, the O₂ column density is $(2.8\text{--}4.3) \times 10^{15}$ cm⁻² assuming ¹⁶O/¹⁸O=550. The inferred abundance ratios are $N(\text{O}_2)/N(\text{C}^{18}\text{O})=1.2$ to 2.1, and $N(\text{O}_2)/N(\text{CO})=(2.2\text{--}3.9) \times 10^{-3}$. Assuming $\text{CO}/\text{H}_2 \approx 10^{-4}$ gives $N(\text{O}_2)/N(\text{H}_2)=(2.2\text{--}3.9) \times 10^{-7}$. Interestingly, the inferred O₂ abundance is in between the values found for the Orion and ρ Oph A clouds (Goldsmith et al. 2011, Liseau et al. 2012).

Can such an O₂ column density and abundance be reproduced by chemical models? For the surrounding cloud, a large gas-grain model is not needed. Instead, the PDR models of Hollenbach et al. (2009), which include a simplified gas-grain chemistry, are adequate to analyse the emission. Figure 6.11 is a plot adapted from Melnick et al. (2012), which shows the values of G_0 required to reproduce the range of O₂ column densities according to the model described in Hollenbach et al. (2009). The horizontal grey band bounds the

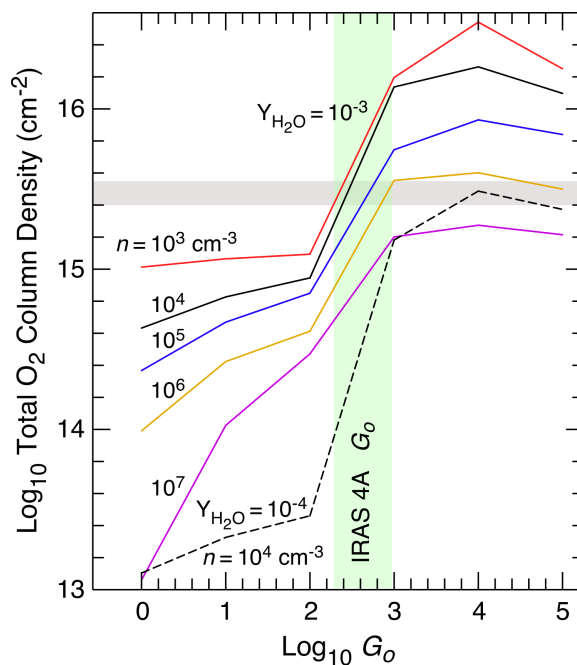


Figure 6.11 – Total O₂ column density as a function of G_0 and density (adapted from Melnick et al. 2012, Hollenbach et al. 2009). The horizontal grey band shows the total O₂ column density range for the observed integrated intensity, whereas the vertical green band presents the range of G_0 values required to produce this range of O₂ column densities for gas densities between 10^3 cm^{-3} and 10^7 cm^{-3} . $Y_{\text{H}_2\text{O}}$ is the water ice photodesorption yield.

total observed O₂ column density range of $(2.8 - 4.3) \times 10^{15} \text{ cm}^{-2}$, while the vertical green band shows the range of G_0 values required to produce this range of O₂ column densities for gas densities between 10^3 cm^{-3} and 10^7 cm^{-3} . For our low inferred densities of $< 10^4 \text{ cm}^{-3}$, a high G_0 value of 300–650 fits the data. A likely scenario for the extended 8.0 km s^{-1} component would be that the UV radiation is enhanced by the nearby B9 V type main sequence star BD+30°549 ($\sim 0.5 \text{ pc}$ away). Models with a water ice photodesorption yield $Y_{\text{H}_2\text{O}} = 10^{-3}$ fit the observations well, consistent with laboratory (Öberg et al. 2009a) and theoretical work (Arasa et al. 2010).

6.6 Conclusions

We have presented the first deep 7.7 hr *Herschel*-HIFI observations of the O₂ 3₃–1₂ line at 487 GHz towards a deeply embedded Class 0 protostar, NGC 1333 IRAS 4A. The results from the observations and models can be summarized as follows.

- No O₂ emission is detected from the protostellar envelope, down to a 3σ upper limit of $X(\text{O}_2) \lesssim 6 \times 10^{-9}$, the lowest O₂ abundance limit toward a protostar to date. The O₂/CO limit is $\leq 5 \times 10^{-3}$.
- A weak line of the chemically related NO molecule is detected at the protostellar velocity of 7.0 km s^{-1} .
- A full gas-grain chemical model coupled with the physical structure of the envelope is compared to our data consisting of two stages, a “pre-collapse stage” and “protostellar stage”. Best fits to the observed upper limit of the O₂ line suggest a long pre-collapse stage (10^6 years), during which atomic oxygen is frozen out onto the dust grains and converted into water ice. Also, at least a fraction of NO must be converted to more complex nitrogen species in the ice.
- The low O₂ abundance in the gas and on the grains implies that the material entering the disk is very poor in O₂.
- A 4.5σ tentative O₂ detection is found at $V_{\text{LSR}} = 8.0 \text{ km s}^{-1}$, which is interpreted as emission originating from the surrounding more extended NGC 1333 cloud.
- Comparison with PDR models of Hollenbach et al. (2009) suggests a high G_0 of 300–650 in the surrounding cloud for the low inferred density of $< 10^4 \text{ cm}^{-3}$.

6.7 Additional materials

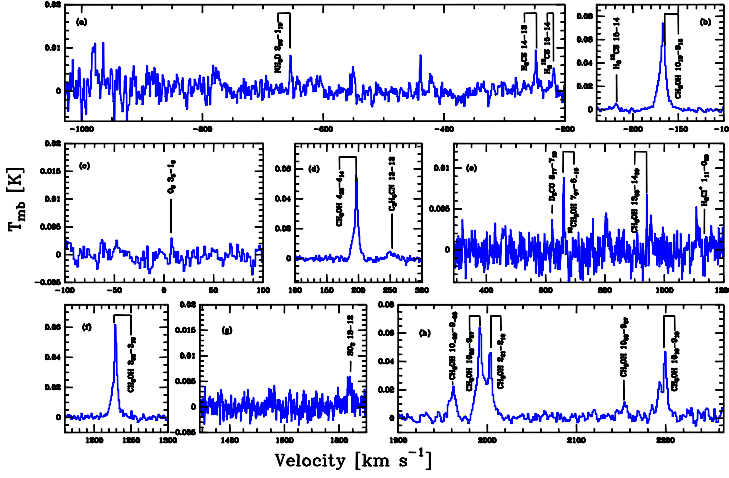


Figure 6.12 – Spectrum of Fig. 6.2 magnified over certain velocity ranges. In panel (c) the O_2 3_3-1_2 transition is shown. Identifications refer to the 7.0 km s^{-1} component.

Table 6.6 – Overview of the other lines observed in the same spectrum.

| Mol. | Trans. J_u-J_l | E_u/k_B [K] | A_{ul} [s^{-1}] | Frequency [GHz] | $\int T_{\text{MB}} dV$ [K km s^{-1}] | T_{peak} [K] | FWHM [km s^{-1}] |
|---------------------------------|---------------------|------------------|---------------------------------|--------------------|--|--------------------------|--------------------------------|
| NH_2D | $2_{02}-1_{10}$ | 47.2 | 1.36×10^{-4} | 488.323810 | 0.025 | 0.01 | 3.4 |
| H_2CS | $14-13$ | 188.8 | 1.76×10^{-3} | 487.663321 | 0.028 | 0.009 | 3.3 |
| H^{13}CS | $15-14$ | 200.5 | 1.77×10^{-3} | 487.615288 | 0.022 | 0.005 | 3.9 |
| CH_3OH | $10_{19}-9_{18}$ | 143.3 | 5.15×10^{-4} | 487.531887 | 0.58 | 0.08 | 8.2 |
| O_2 | 3_3-1_2 | 26.38 | 8.66×10^{-9} | 487.249264 | 0.007 | ... | ... |
| CH_3OH | $4_{23}-4_{14}$ | 60.9 | 5.45×10^{-4} | 486.940837 | 0.39 | 0.06 | 7.2 |
| $\text{C}_2\text{H}_5\text{CN}$ | $13-12$ | 66.9 | 1.00×10^{-6} | 486.849912 | 0.036 | 0.005 | 7.3 |
| D_2CO | $8_{17}-7_{16}$ | 111.0 | 3.36×10^{-3} | 486.248662 | 0.009 | 0.007 | 1.1 |
| $^{13}\text{CH}_3\text{OH}$ | $7_{07}-6_{16}$ | 76.5 | 3.02×10^{-4} | 486.188242 | 0.039 | 0.01 | 3.9 |
| CH_3OH | $13_{68}-14_{59}$ | 404.8 | 1.16×10^{-4} | 485.732280 | 0.012 | 0.01 | 1.4 |
| H_2Cl^+ | $1_{11}-0_{00}$ | ... | ... | 485.420796 | -0.005 | -0.006 | 0.8 |
| CH_3OH | $3_{22}-3_{13}$ | 51.6 | 5.02×10^{-4} | 485.263263 | 0.401 | 0.071 | 7.3 |
| SO_2 | $13-12$ | 105.8 | 5.42×10^{-4} | 484.270879 | 0.026 | 0.006 | 1.1 |
| CH_3OH | $10_{-29}-9_{-28}$ | 153.6 | 4.88×10^{-4} | 484.071775 | 0.17 | 0.02 | 8.4 |
| CH_3OH | $10_{28}-9_{27}$ | 150.0 | 4.83×10^{-4} | 484.023168 | 0.49 | 0.07 | 8.2 |
| CH_3OH | $2_{21}-2_{12}$ | 44.7 | 3.99×10^{-4} | 484.004740 | 0.28 | 0.05 | 4.9 |
| CH_3OH | $10_{28}-9_{27}$ | 165.4 | 4.90×10^{-4} | 483.761387 | 0.07 | 0.01 | 5.8 |
| CH_3OH | $10_{19}-9_{18}$ | 148.7 | 5.13×10^{-4} | 483.686308 | 0.21 | 0.05 | 4.2 |

Notes: *rms* is 1.3 mK in 0.35 km s^{-1} bin. Identifications refer to the 7.0 km s^{-1} component.

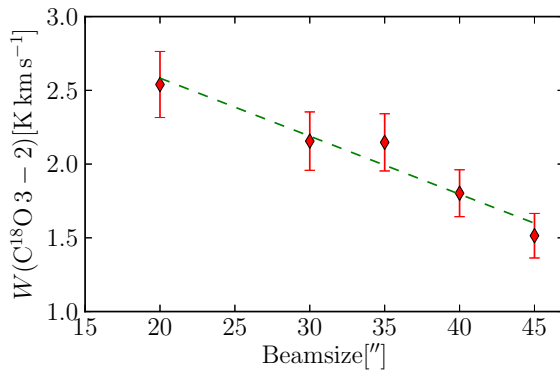


Figure 6.13 – Integrated on source C¹⁸O 3–2 intensities when map is convolved to different beam sizes and corresponding intensities are measured. The intensity decreases by a factor of 0.6 with increasing beam size (20'' to 44'').

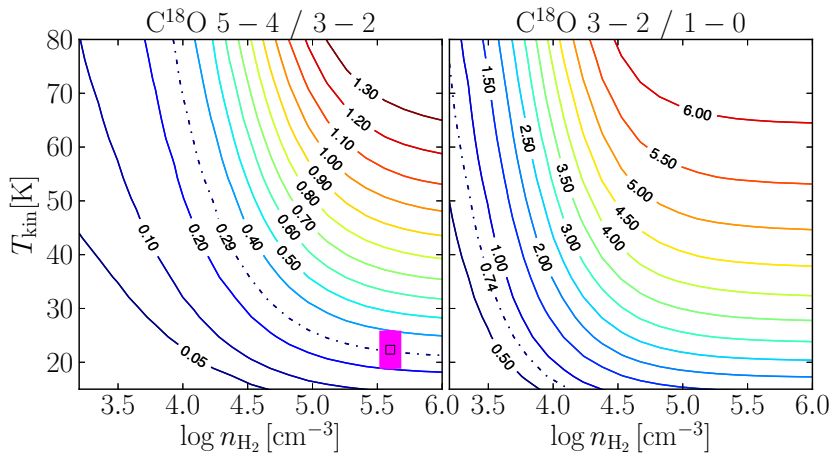


Figure 6.14 – Integrated intensity ratios calculated with RADEX, as function of temperature and density, for a C¹⁸O column density of $5 \times 10^{14} \text{ cm}^{-2}$ (optically thin conditions). The C¹⁸O 5–4/3–2 ratio is representative for the IRAS 4A envelope which is traced by the 7.0 km s^{-1} component; the C¹⁸O 3–2/1–0 ratio is representative for the surrounding NGC 1333 cloud, which is traced by the 8.0 km s^{-1} component. Dash-dotted lines indicate the observed ratios of C¹⁸O 5–4/3–2=0.29 and C¹⁸O 3–2/1–0=0.74 for the $V_{\text{LSR}}=7.0$ and 8.0 km s^{-1} components, respectively. The purple bar in the left figure indicates the IRAS 4A density at the $44''/2$ radius.

Acknowledgements

UAY and astrochemistry in Leiden are supported by the Netherlands Research School for Astronomy (NOVA), by a Spinoza grant and grant 614.001.008 from the Netherlands Organisation for Scientific Research (NWO), and by the European Community's Seventh Framework Programme FP7/2007-2013 under grant agreement 238258

(LASSIE) and 291141 (CHEMPLAN). This work was carried out in part at the Jet Propulsion Laboratory, which is operated by the California Institute of Technology under contract with NASA. The authors are grateful to many funding agencies and the HIFI-ICC staff, who has been contributing for the construction of Herschel and HIFI for many years. HIFI has been designed and built by a consortium of institutes and university departments from across Europe, Canada and the United States under the leadership of SRON Netherlands Institute for Space Research, Groningen, The Netherlands and with major contributions from Germany, France and the US. Consortium members are: Canada: CSA, U.Waterloo; France: CESR, LAB, LERMA, IRAM; Germany: KOSMA, MPIfR, MPS; Ireland, NUI Maynooth; Italy: ASI, IFSI-INAF, Osservatorio Astrofisico di Arcetri-INAF; Netherlands: SRON, TUD; Poland: CAMK, CBK; Spain: Observatorio Astronómico Nacional (IGN), Centro de Astrobiología (CSIC-INTA). Sweden: Chalmers University of Technology - MC2, RSS & GARD; Onsala Space Observatory; Swedish National Space Board, Stockholm University - Stockholm Observatory; Switzerland: ETH Zurich, FHNW; USA: Caltech, NASA/JPL, NHSC.

